Inorganic Chemistry

Article

pubs.acs.org/IC

Actinide Oxidation State and O/M Ratio in Hypostoichiometric Uranium−Plutonium−Americium $U_{0.750}Pu_{0.246}Am_{0.004}O_{2-x}$ Mixed Oxides

Romain Vauchy,[†] Renaud C. Belin,[‡] Anne-Charlotte Robisson,[‡] Florent Lebreton,[†] Laurence Aufore,[‡,§] Andreas C. Scheinost,[∥,⊥] and Philippe M. Martin*[,†,‡]

[†]CEA, DEN, DTEC, Centre d'études nucléaires de Marcoule, Bagnols-sur-Cèze F-30207, France

[‡]CEA, DEN, DEC, Centre d'études nucléaires de Cadarache, Saint Paul Lez Durance F-13108, France

[§]CEA, DEN, DTN, Centre d'études nucléaires de Cadarache, Saint Paul Lez Durance F-13108, France

[∥]Helmholtz Zentrum Dresden-Rossendorf (HZDR), Institute of Resource Ecology, P.O. Box 510119, 01314 Dresden, Germany

[⊥]BM20 Rossendorf Beamline at European Synchrotron Radiation Facility, BP 220, F-38043 Grenoble, France

ABSTRACT: Innovative americium-bearing uranium−plutonium mixed oxides $U_{1-y}Pu_yO_{2-x}$ are envisioned as nuclear fuel for sodium-cooled fast neutron reactors (SFRs). The oxygen-to-metal (O/M) ratio, directly related to the oxidation state of cations, affects many of the fuel properties. Thus, a thorough knowledge of its variation with the sintering conditions is essential. The aim of this work is to follow the oxidation state of uranium, plutonium, and americium, and so the O/M ratio, in $U_{0.750}Pu_{0.246}Am_{0.004}O_{2-x}$ samples sintered for 4 h at 2023 K in various Ar + 5% H_2 + z vpm H_2O (z = ∼15, ∼90, and ∼200) gas mixtures. The O/M ratios were determined by gravimetry, XAS, and XRD and evidenced a partial oxidation of the samples at room temperature. Finally, by comparing XANES and EXAFS results to that of a previous study, we demonstrate that the presence of uranium does not influence the interactions between americium and plutonium and that the differences in the O/M ratio between the investigated conditions is controlled by the reduction of plutonium. We also discuss the role of the homogeneity of cation distribution, as determined by EPMA, on the mechanisms involved in the reduction process.

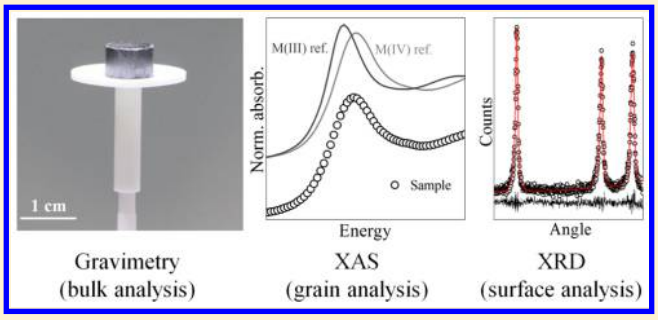

1. INTRODUCTION

Uranium−plutonium mixed oxide fuels $U_{1-y}Pu_yO_{2-x}$ are currently studied within the frame of the fourth generation (GEN-IV) of nuclear reactors and more precisely, for sodium-cooled fast neutron reactors (SFRs). GEN-IV's main purpose is managing more efficiently the energetic resources by recycling valuable actinides such as U and Pu from spent nuclear fuels. Because of their specific neutronic spectrum, SFRs will also be able to burn long-lived minor actinides (MAs) such as Am, Np, and Cm recovered from spent nuclear fuel. This could lead to a drastic decrease in both radiotoxicity and heat load of ultimate glassy wastes favoring the ecological footprint of their final disposal.[1] Among MAs, Am is of main concern. Two options are considered: (a) homogeneous transmutation by introducing small amounts (2−5%) of MAs into the $U_{1-y}Pu_yO_{2-x}$ mixed oxide fuel[1−5] or (b) heterogeneous transmutation by introducing Am in higher concentration into an inert matrix[1−4,6−8] or fertile UO_2 blankets.[1,9,10] Regarding the first option, uranium−plutonium mixed oxide fuel incorporating up to 5% AmO_2 is a promising candidate.[1]

Because the oxygen stoichiometry significantly affects most of the fuel properties (thermal conductivity, melting temperature, diffusion phenomena, fuel/cladding interactions, etc.),[11−13] studying the oxygen/metal (O/M) ratio of MA-bearing mixed oxides is necessary. According to currently identified specifications, the O/M ratio of the SFR's fuel will have to range from 1.94 to 2.00. Controlling the O/M ratio of the future $U_{1-y}Pu_yO_{2-x}$ nuclear fuel during its manufacturing remains highly challenging and depends upon several fabrication factors (sintering atmosphere, homogeneity of cation distribution, cooling rate, storage duration and conditions, etc.), as illustrated by our recent publications.[14−21] Therefore, a thorough knowledge of the correlation between the sintering atmosphere (and the associated oxygen potential) and O/M ratio is a major concern. Osaka et al.[22] have highlighted discrepancies between modeled and experimental oxygen potential vs O/M ratio curve for Am-bearing uranium−plutonium mixed oxide $U_{0.685}Pu_{0.270}Am_{0.045}O_{2-x}$. Previous experimental studies have revealed a discontinuity in the relationship between both parameters that may be attributed either to a nonconcurrent reduction of americium and plutonium[23] or to an interaction between Am and Pu oxides.[24] The oxygen potential of AmO_{2-x} is much higher than that of PuO_{2-x} for a given O/M ratio.[25] As a

Received: November 3, 2015
Published: February 23, 2016

DOI: 10.1021/acs.inorgchem.5b02533
Inorg. Chem. 2016, 55, 2123−2132

consequence, different U−Pu and U−Am charge distribution are obtained in the respective mixed oxides for similar sintering conditions. Contrary to Am, which was shown to be purely trivalent in uranium−americium mixed oxides,[26−28] Pu(III) does not coexist with U(V) because it is fully reoxidized to Pu(IV) before pentavalent uranium is formed.[21] Such a behavior implies that Am should be more readily reduced than Pu in (U, Pu, Am)O_{2-x} compounds. Moreover, as we already evidenced in a previous study,[29] pure AmO_2 can be reduced to $AmO_{1.62}$. This may occur before starting to reduce plutonium in PuO_2.[24] The different behavior of Am and Pu cations might be responsible for the unusual oxygen potential vs O/M ratio relationship in Am-bearing uranium−plutonium mixed oxides evidenced by Osaka et al.[22,23]

The aim of the present study is to better understand the mechanisms involved in the reduction of americium and plutonium cations in (U, Pu, Am)O_{2-x} for selected O/M ratios and, subsequently, to provide insight into the oxygen potential vs O/M ratio correlation. Combining gravimetric analysis, X-ray diffraction (XRD), and X-ray absorption spectroscopy (XAS) proved to be a relevant method to both quantitatively determine the cation oxidation states (through XANES) and highlight discrepancies between local (EXAFS) and long-range (XRD) structural modifications.[30−32] Furthermore, since these techniques allow probing different depths, their association makes it possible to estimate how the stoichiometry of the analyzed samples varies from the surface of the material to its bulk.[21]

Because neither metal vacancies nor interstitials are expected in single and mixed actinide oxides, the O/M ratio of nuclear fuel relies mainly on the oxidation state of its constitutive actinide cations. Thus, the goal of the present work was to study uranium, plutonium, and americium cations, and in particular their oxidation states, in $U_{0.750}Pu_{0.246}Am_{0.004}O_{2-x}$ samples as a function of the moisture content of the sintering atmosphere Ar + 5% H_2 + z vpm H_2O (z = ∼15, ∼90, and ∼200).

2. EXPERIMENTAL SECTION

2.1. Sample Preparation. In this study, uranium dioxide and plutonium dioxide powders were used. The uranium dioxide powder was produced by a wet fabrication route based on the formation of ammonium diuranate from uranyl nitrate precipitated with ammonia. The obtained particles were then atomized, dried, and calcined, leading to spherical-shaped agglomerates of around 20 μm in diameter. Plutonium dioxide powder was produced by precipitation of a plutonium nitrate solution within oxalic acid to form plutonium oxalate. The particles were heated in air at 923 K and parallelepiped-shaped PuO_2 particles were obtained with an average size of 15 μm.

Uranium−plutonium mixed oxide samples were obtained by a powder metallurgy process consisting of mixing 75 mol % UO_2 with 25 mol % PuO_2 at the LEFCA facility (CEA Cadarache, France). The americium present in the samples was due to the β-decay of ^{241}Pu within the raw PuO_2 powder. Because the amount of ^{241}Pu isotope was 2.91% when the PuO_2 powder was synthesized in 1995, its decay generated an Am/(Am + Pu) ratio close to 1.5% when the present study was performed. As a consequence, the overall americium concentration Am/Metal in the studied samples was ∼0.4% leading to the $U_{0.750}Pu_{0.246}Am_{0.004}O_2$ composition. The obtained mixture was then micronized by comilling for 2 h in a ball-mill and subsequently passed through a metallic sieve (160 μm grids). With the prospect of preventing the introduction of metallic particles within the samples, it was chosen not to force on the powder while sieving. The resulting powder exhibited a BET specific surface area of 6.2 $m^2 \cdot g^{-1}$ with apparent and packed densities equal to 2.9 and 3.7 $g \cdot cm^{-3}$, respectively. The powder was then pressed into pellets with an automatic uniaxial, monopunch press equipped with a floating matrix. The applied pressure was constant for all the pellets and equal to ∼400 MPa. No lubricants were added to the powders. A similar fabrication process is detailed elsewhere.[33] The resulting green pellets were subsequently sintered at 2023 K for 4 h with heating and cooling rates both set at ∼0.03 $K \cdot s^{-1}$ under three different Ar + 5% H_2 + z vpm H_2O atmospheres (z = ∼15, ∼90, and ∼200). The resulting samples exhibited a high apparent density ranging from 96 to 98% of the theoretical density, as determined by the hydrostatic method. The moisture content of the sintering gas mixture was measured at room-temperature with a capacitive probe. The associated oxygen potentials $\Delta\bar{G}_{O_2}$ at 2023 K were computed using the latest standard thermodynamic properties taken from reference.[34] If one considers equilibrium (1), eqs 2 to 5 can be deduced:

$$\frac{1}{2}O_2 + H_2 \leftrightharpoons H_2O \quad (1)$$

$$\frac{1}{2}\mu_{O_2} + \mu_{H_2} = \mu_{H_2O} \quad (2)$$

with μ_X the chemical potential of the species X.

$$\mu_{O_2} = \mu^0_{O_2} + R \cdot T \cdot \ln(pO_2) \quad (3)$$

$$\mu_{H_2} = \mu^0_{H_2} + R \cdot T \cdot \ln(pH_2) \quad (4)$$

$$\mu_{H_2O} = \mu^0_{H_2O} + R \cdot T \cdot \ln(pH_2O) \quad (5)$$

with pX the partial pressure of the species X (bar), R the gas constant (taken equal to 8.314 $J \cdot mol^{-1} \cdot K^{-1}$) and T the temperature expressed in K. One can get eq 6:

$$\mu^0_X = \Delta\bar{G}^0_{fX} \quad (6)$$

where $\Delta\bar{G}^0_{fX}$ is the free energy of formation (kJ mol^{-1}) of the species X at a given temperature. We also have eq 7:

$$\Delta\bar{G}^0_{fX} = \Delta\bar{H}^0_{fX} - T\Delta\bar{S}^0_{fX} \quad (7)$$

The standard thermodynamic properties $\Delta\bar{H}^0_{fX}$ (kJ mol^{-1}) and $\Delta\bar{S}^0_{fX}$ (J $mol^{-1} \cdot K^{-1}$) of the three considered species involved in equilibrium (1) were determined according to eqs 8 and 9.

$$\Delta\bar{H}^0_{fX} = A \cdot t + \frac{B}{2} \cdot t^2 + \frac{C}{3} \cdot t^3 - \frac{D}{4} \cdot t^4 - \frac{E}{t} + F \quad (8)$$

Table 1. Thermodynamic Coefficients Determined at 2023 K from Reference 34 for the Three Considered Gaseous Species

	O_2(g)	H_2(g)	H_2O(g)
A	20.91111	18.563083	41.96426
B	10.72071	12.257357	8.622053
C	−2.020498	−2.859786	−1.499780
D	0.146449	0.268238	0.098119
E	9.245722	1.977990	−11.15764
F	5.337651	−1.147438	−272.1797
G	237.6185	156.288133	219.7809

Table 2. Calculation of the Oxygen Potentials at 2023 K under Ar + 5% H_2 + z vpm H_2O

z (vpm)	pH_2O/pH_2	pO_2 (bar)	$\Delta\bar{G}_{O_2}$ (kJ mol^{-1})
∼200	0.0040	$\sim 1.9.10^{-12}$	−450
∼90	0.0018	$\sim 3.8.10^{-13}$	−470
∼15	0.0003	$\sim 1.0.10^{-14}$	−500

In this paper, the samples will be referenced by their respective oxygen potential at 2023 K given in Table 2, i.e. −450, −470, and −500 kJ mol^{-1}.

DOI: 10.1021/acs.inorgchem.5b02533
Inorg. Chem. 2016, 55, 2123−2132

$$\Delta\bar{S}^0_{fX} = A\cdot\ln(t) + B\cdot t + \frac{C}{2}\cdot t^2 + \frac{D}{3}\cdot t^3 - \frac{E}{2t^2} + G \quad (9)$$

with A, B, C, D, E, F, and G the thermodynamic coefficients given in Table 1 determined at 2023 K according to reference[34] and with t = temperature (K)/1000.

From equilibrium (1), one can conclude:

$$R\cdot T\cdot\ln\left(\frac{pH_2O}{pH_2\cdot pO_2^{1/2}}\right) = -\Delta\bar{G}^0_r \quad (10)$$

with the following expression of the free energy of reaction:

$$-\Delta\bar{G}^0_r = -\mu^0_{H_2O} + \mu^0_{H_2} + \frac{1}{2}\mu^0_{O_2} \quad (11)$$

Then:

$$\frac{pH_2O}{pH_2\cdot pO_2^{1/2}} = \exp\left(\frac{-\mu^0_{H_2O} + \mu^0_{H_2} + \frac{1}{2}\mu^0_{O_2}}{R\cdot T}\right) \quad (12)$$

$$\Delta\bar{G}_{O_2} = R\cdot T\cdot\ln(pO_2) \quad (13)$$

We finally obtain the oxygen potentials $\Delta\bar{G}_{O_2}$ at 2023 K given in Table 2.

2.1. Apparatus and Experimental Technique. Electron Probe Micro Analysis (EPMA) was performed with a CAMECA SX50 device equipped with a tungsten source. For each microstructure, three X-ray mappings of 1024 × 1024 pixels (1 μm^2 for each pixel) randomly selected were collected using the displacement mode of the sample holder stage. The analysis conditions are 20 kV for electron accelerating voltage, giving an analysis volume of 1 μm^3, and 80 nA for beam current. Measurements were carried out on the Pu Mβ, U Mα (using PET ($C_5H_{12}O_4$) crystals) and O Kα (using a PC1 (W/Si) multilayer crystal) peaks without subtracting the background.[35] The selected counting time was about 20 ms per pixel, which represented approximately 6 h of data acquisition per map. Quantitative measurements were also performed along 700 μm long lines, randomly chosen in each map with step of 1 μm, using UO_2 and PuO_2 reference compounds for U and Pu, respectively. The comparison of the Pu mapping and quantitative results allow a semiquantification of the plutonium distribution. Because the lack of reference material and its low concentration within the considered samples, americium was not directly analyzed by EPMA.

As described in reference,[21] bulk-scale O/M ratio measurements were performed by gravimetric method using an ADAMEL furnace coupled with a gas-mixing device allowing the control of the atmosphere, and more precisely, its oxygen partial pressure pO_2 as a function of temperature. Oxygen partial pressures were controlled via the moisture content of an Ar + 5% H_2 gas mixture and set by diverting a fraction of the Ar/H_2 flow through water maintained at 288 K and measured, at room-temperature, with a capacitive probe. Thermal treatments at 1173 K for 24 h under Ar + 5% H_2 + ~24 000 vpm H_2O were applied to the hypostoichiometric mixed oxide pellets. According to both thermodynamic model proposed by Guéneau et al.[36] and diffusion model proposed by Moore et al.[37] currently under development for uranium−plutonium mixed oxides, these conditions lead to stoichiometric samples (O/M = 2.000 ± 0.001) at room temperature. By comparing the initial mass of the pellet to that after the thermal treatment and by considering a final stoichiometry of 2.000, the initial O/M ratio can be calculated by using eq 14 with an accuracy of ±0.001. The latter is obtained by taking into account the repeatability of the experiment with other pellets of the same batch, and the stoichiometry was checked again with a NETZSCH Jupiter STA 449C thermobalance coupled to a similar moisture control device.

$$\frac{O}{M} = 2 \pm x = 2 \pm \frac{M_{U_{1-y-z}Pu_{y-z}Am_zO_2}}{M_O}\cdot\frac{|m_f - m_i|}{m_f} \quad (14)$$

with the following:

- (O/M): initial oxygen-to-metal ratio of $U_{1-y-z}Pu_{y-z}Am_zO_{2\pm x}$
- x: deviation from stoichiometry
- $M_{U_{1-y-z}Pu_{y-z}Am_zO_2}$: molar mass (g mol^{-1}) of $U_{1-y-z}Pu_{y-z}Am_zO_{2.000}$ (taking into account the isotopic composition of uranium, plutonium, and americium)
- M_O: molar mass of oxygen
- m_f: mass of $U_{1-y-z}Pu_{y-z}Am_zO_{2.000}$
- m_i: initial mass of $U_{1-y-z}Pu_{y-z}Am_zO_{2\pm x}$

All XRD measurements were performed at atmospheric pressure and room temperature with a Bragg−Brentano θ-2θ SIEMENS D5000 X-ray diffractometer using a curved quartz monochromator and copper radiation from a conventional tube source (Kα_1 radiation, λ = 1.5406 Å). Powder diffraction patterns were obtained by scanning from 25° to 140° 2θ using 0.02° step-intervals and counting time of 0.2 s per step. The procedure is thoroughly described by Belin et al.[38] Because the X-rays generated by the XRD only penetrate a thin layer (roughly 1 μm) in the uranium-plutonium-americium mixed oxides, the analysis made it possible to probe the surface of the grains.[21] Whole powder pattern decomposition was realized according to the Pawley method[39] using DIFFRAC^{plus} TOPAS v4 software.[40] The obtained results allow calculating the O/M ratio (= 2-x with x the deviation from stoichiometry) (±0.003) of each phase constituting the material at room temperature with an empirical correlation (15) connecting the lattice parameter (a in pm), the plutonium content (y = Pu/Metal) and the deviation from stoichiometry (x):[13]

$$a(\text{pm}) = 547 - 7.4y + 32x \quad (15)$$

XAS measurements were performed at the Rossendorf Beamline (BM20) located at the European Synchrotron Radiation Facility (ESRF, Grenoble, France). Storage ring operation conditions were 6.0 GeV and 170−200 mA. The beam was conditioned using a double crystal monochromator with Si (111) crystals for monochromatization and two Pt-coated mirrors for collimation and reduction of higher harmonics. XAS using high energy light source generated with a synchrotron, the probed depth in $U_{1-y-z}Pu_{y-z}Am_zO_2$ compounds is equal to tens of microns.[24] Because the grain size of the fabricated samples was the same scale as the synchrotron X-rays probing depth, the whole grains were then illuminated by the X-ray source. XAS samples were prepared by mixing about 1 mg of material (obtained by manually crushing a dense pellet) with 20 mg of boron nitride. Samples were then pressed into a thin bar inserted into a hermetic Teflon/polyethylene sample holder. Sample holders were mounted in a closed-cycle He cryostat running at 15 K in order to avoid the thermal vibration contributing to the Debye−Waller factors of EXAFS spectra, which can then be considered as only influenced by static structural disorder. Spectra at U-L_{III} edge (17 166 eV) were collected in transmission mode, whereas those for plutonium were recorded in fluorescence mode using a 13-element Ge detector at L_{II} edge (22 666 eV) because, as we previously observed,[41] the Pu-L_{III} edge is distorted by the uranium L_{III} EXAFS signal. Considering the low Am concentration and the nearby Pu-L_I edge position (23 108 eV), only XANES spectra were collected at the Am-L_{II} edge (22 952 eV).[17] The spectra were corrected for dead time using a measured relationship between the incoming count rate and selected channel analyzer readings for each channel by using the SixPack software package. This procedure ensured that the absorption peak height matched the transmission data. Energy calibrations were performed using a Y foil (17 038 eV) or a Mo foil (20 000 eV) positioned after the second ionization chamber. The ATHENA software[42] was used for normalizing XANES spectra. The E_0 values were taken at the first inflection point using the first zero-crossing value of the second derivative. The position of white line maximum was determined by the first zero-crossing of the first derivative. UO_2, PuO_2, and AmO_2 were considered as reference for tetravalent uranium,[17,43,44] plutonium,[17,24,45,46] and americium,[27] whereas $(N_2H_5^+)_{1.2}(H_3O^+)_1U_{1.8}Pu_{0.2}(C_2O_4)_5$, $n$$H_2O$ mixed oxalate (denominated as "oxalate" in this paper) and $Am_2Zr_2O_7$ pyrochlore were used as reference for trivalent plutonium[47] and americium,[30] respectively. Experimental XANES data were fitted between −20 and +30 eV compared to the E_0 position using linear combination of spectra collected on reference compounds. The goodness of the fit was estimated with both R factor and χ^2 values. XANES results allowed

DOI: 10.1021/acs.inorgchem.5b02533
Inorg. Chem. 2016, 55, 2123−2132

determining O/M ratios with an accuracy of ±0.01. The ATHENA software was also used for extracting EXAFS oscillations from the raw absorption spectra. Experimental EXAFS spectra were Fourier transformed using a Hanning window over the full k space range available for each edge. Curve fitting was performed in k^{1-3} space for R-values for all edges. Phases and amplitudes for the interatomic scattering paths were calculated with the *ab initio* code FEFF8.40[48] based on a defect free fluorite structure model in which each cation is surrounded by 8 oxygen anions at $a \times \sqrt{3}/4$, 12 cations at $a \times \sqrt{2}/2$, and 24 oxygen anions at $a \times \sqrt{11}/4$ (a being the lattice parameter determined by XRD).

3. RESULTS AND DISCUSSION

Quantification of Homogeneity of Cation Distribution. EPMA showed that the three samples exhibited similar homogeneities of cation distribution. In all cases, some local U-rich and Pu-rich zones of roughly 30−70 μm and ≤20 μm in size, respectively. Even if the Pu-rich zones were of smaller size, their quantity was more important. An example is given in Figure 1.

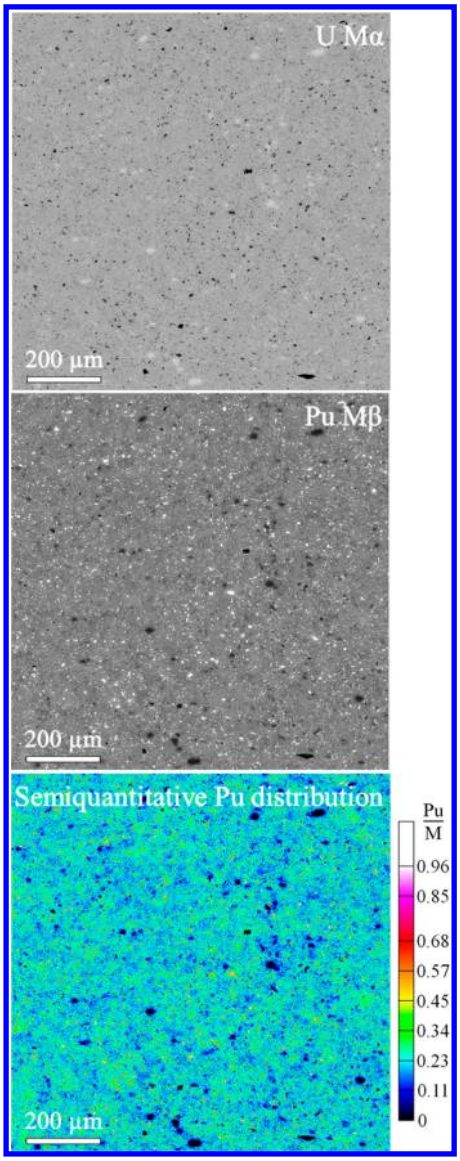

Figure 1. EPMA X-ray mapping (1024 × 1024 μm^2) for the distribution of uranium and plutonium (arbitrary gray scale) and associated semiquantitative Pu distribution in $U_{0.750}Pu_{0.246}Am_{0.004}O_{2-x}$.

From the semiquantitative Pu mapping given in Figure 1, the surface distribution as a function of the plutonium content was determined in order to estimate its associated homogeneity of distribution and is given in Figure 2.

The plutonium content y = Pu/M exhibited a broad unimodal distribution centered on y = 0.243 throughout the analyzed areas. The low surface fractions of pure UO_2 and y > 0.5 evidenced a relatively good dissolution of the initial raw materials in favor of the formation of intermediate mixed oxides whose plutonium content is given in Figure 2. These results then strengthened the accuracy in manufacturing the samples, especially in obtaining the average plutonium content target value of y = 0.246.

Determination of O/M Ratios of Bulk Samples. Gravimetric O/M ratio measurements were performed on ∼2 g dense pellets directly after sintering. Results are shown in Table 3.

For a given sintering step (heating/cooling rates, dwell duration, and temperature), the measured O/M ratios reported in Table 3 mirror the decrease in the moisture content of the processing gas mixture, i.e. in lowering the oxygen potential at a given temperature. This observation is in agreement with previous results[20] and also with thermodynamic calculations (Figure 3) performed by employing the Thermo-Calc Software[49] and the thermodynamic model proposed by Guéneau et al.[36] Indeed, for a given equilibrium of $U_{0.75}Pu_{0.25}O_{2-x}$ at a fixed temperature, decreasing the oxygen potential (i.e., the moisture content of the processing gas mixture) involves a drop in the reciprocal O/M ratio. During cooling from sintering to room temperature, an oxidation of the samples up to O/M = 2.000 is expected when reaching thermodynamic equilibrium.[17,20,33,50] Because this oxidation is a process mediated by surface diffusion and because the sintered samples are pellets, thermodynamic equilibrium between materials and surrounding gas phase is hardly achieved,[19,20] allowing obtaining hypostoichiometric mixed oxides at room-temperature. As a consequence, the deviation from stoichiometry measured for each sample corresponds to an intermediate "frozen" state between sintering and room temperature. Nevertheless, the tendency illustrated in Figure 3 connecting the moisture content of the gas mixture to the O/M ratio is preserved even at room temperature. Then, even out of equilibrium, the O/M ratio of $U_{1-y}Pu_yO_{2-x}$ mixed oxide pellets at room-temperature relies on both sintering atmosphere and cooling rate.

Determination of Long-Range Structural Properties. XRD analysis was performed on a manually crushed sample of each set. A slight shoulder was observed on the high-angles region of the XRD patterns collected on the −500 kJ mol^{-1} sample as a consequence of the possible presence of a second phase indexed by red arrows in Figure 4. Since this feature was only observed on the −500 kJ mol^{-1} and because the samples sintered under the three atmospheres presented very similar EPMA results, this second phase is not considered as a fabrication artifact but can be related to a consequence of a demixing process. Indeed, as evidenced in previous studies,[17−20,52] a phase separation is expected in this composition range (Pu content and sintering conditions). The two phases constituting the hypostoichiometric mixed oxides exhibit different oxygen contents and are then called "high-oxygen" and "low-oxygen" phases, respectively.[17−21,52] Because of the relatively low plutonium content of the present samples, regarding the Pu composition range of the miscibility gap existing in the UO_2−PuO_2−Pu_2O_3 subsystem (i.e., $0.2 \leq y \leq 1$), the composition of the two phases within the miscibility gap is

DOI: 10.1021/acs.inorgchem.5b02533
Inorg. Chem. 2016, 55, 2123−2132

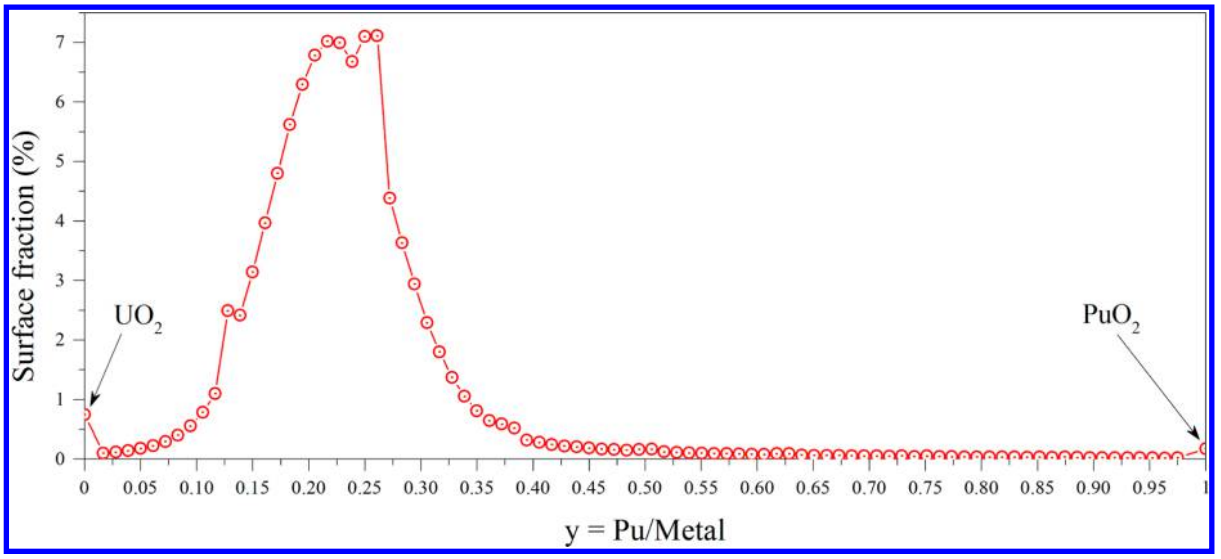

Figure 2. Surface fraction of distribution of plutonium content (y = Pu/Metal) ranges.

Table 3. O/M Ratios of the Three $U_{0.750}Pu_{0.246}Am_{0.004}O_{2-x}$ Samples As Determined by Gravimetric Measurements

oxygen potential at 2023 K (kJ mol^{-1})	measured O/M ratio
−450	1.983(1)
−470	1.974(1)
−500	1.937(1)

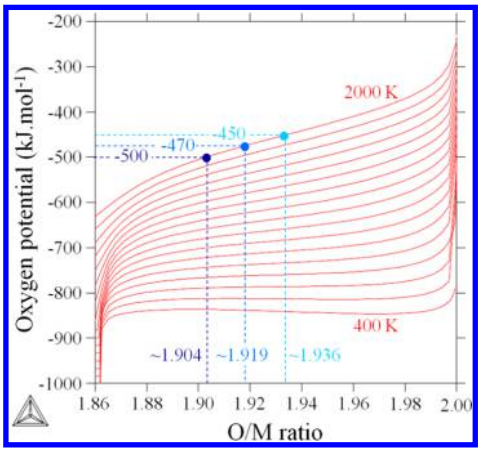

Figure 3. Variation in the oxygen potential of $U_{0.75}Pu_{0.25}O_{2-x}$ as a function of O/M ratio for various temperatures ranging from 400 to 2000 K by steps of 100 K, replotted from ref 51.

too close one to the other to be reasonably distinguished. Furthermore, the second (low-oxygen) phase is hardly observable. As a consequence, a Rietveld refinement, eventually leading to the determination of the fraction of the two phases constituting the −500 kJ mol^{-1} sample, is not reliable. Moreover, as evidenced in one of our previous studies,[21] the monophasic nature of the samples could also be explained by a partial oxidation process at room temperature involving the almost complete disappearance of the low-oxygen phase. For these reasons, the three samples were considered as exhibiting a monophasic structure (Figure 4) indexed in the $Fm\bar{3}m$ face-centered cubic space-group. The lattice parameters given in Table 4 then correspond to average values considered as representative of the samples and ultimately allowed evaluating their O/M ratio from relation (15).

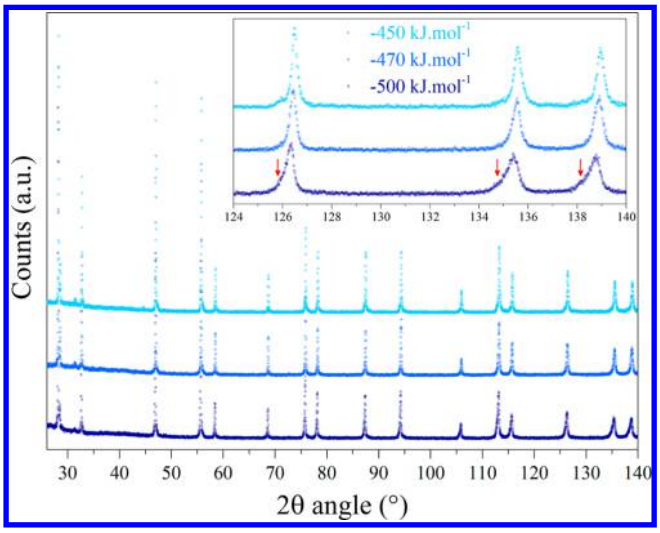

Figure 4. XRD patterns of the three $U_{0.750}Pu_{0.246}Am_{0.004}O_{2-x}$ samples. The possible second phase in the −500 kJ mol^{-1} sample is referenced with red arrows in the zoomed section.

Table 4. Lattice Parameters Obtained with the Pawley Method and O/M Ratios Calculated from Relation (2)

oxygen potential at 2023 K (kJ mol^{-1})	lattice parameter (Å)	calculated O/M ratio
−450	5.456(1)	1.987(3)
−470	5.457(1)	1.984(3)
−500	5.458(1)	1.977(3)

Because the X-rays generated by the XRD device only penetrate a thin layer (roughly 1 μm) in actinide oxides, in contrast to gravimetric measurements that probe the whole bulk of the sample, the calculated O/M ratios at room-temperature from lattice parameters of $U_{0.750}Pu_{0.246}Am_{0.004}O_{2-x}$ do not match those given in Table 3 as a consequence of a surface oxidation.[21] However, the tendency of the variation in O/M ratio with the oxygen potential is preserved.

If one considers that the detection limit of conventional laboratory XRD is ∼4%, EPMA results given in Figure 2 can be analyzed in order to evaluate a hypothetical XRD peak

DOI: 10.1021/acs.inorgchem.5b02533
Inorg. Chem. 2016, 55, 2123−2132

Table 5. Calculated Lattice Parameters with the Distribution of Plutonium Determined by EPMA (Surface Fraction >4%)

	y = Pu/(U+Pu)										
	0.161	0.172	0.183	0.194	0.205	0.216	0.227	0.239	0.250	0.261	0.272
lattice parameter (Å)	5.458	5.457	5.456	5.456	5.455	5.454	5.453	5.452	5.451	5.451	5.450

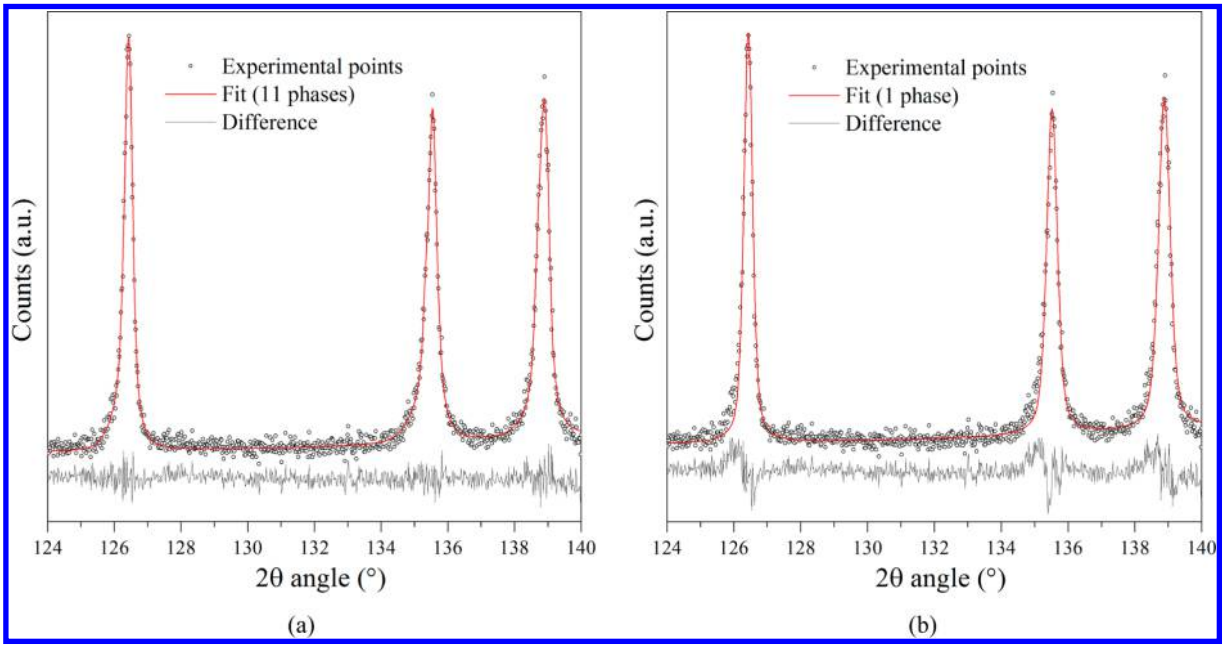

Figure 5. Illustration of the effect of the distribution of plutonium determined by EPMA on the fit of a given XRD pattern: (a) fit with the 11 phases given in Table 4 and (b) fit with one phase.

Table 6. Influence of the Number of Phases Taken into Account for Fitting the XRD Data on the Refinement Results

number of phases in the fit	R_{wp}	R_p	GoF
11	13.79	9.42	1.29
1	15.41	11.35	1.43

broadening due to cation distribution. Thus, the lattice parameter of each intermediate $U_{1-y}Pu_yO_2$ mixed oxide was calculated with Vegard's law between UO_2 and PuO_2 with relation (2). As an approximation, no deviation from stoichiometry was taken into account in the calculation. Only plutonium contents representing a surface fraction greater than 4% in Figure 2 were considered.

Once these lattice parameters were determined, a new refinement of the XRD patterns was performed in order to estimate the impact of the 11 intermediate phases given in Table 5 on the fit. The resulting fit given in Figure 5 (a) is compared to a refinement performed with only one phase (Figure 5b). To exacerbate a potential effect of the distribution of plutonium on the fit, and for clarity reasons, only a restricted angular section (at high angles: 124°−140°2θ) is shown in Figure 5. Associated refinement results of XRD data (R_{wp} weighted profile, R_p profile, and GoF goodness of fit) are given in Table 6.

As it clearly appears in Figure 5 and Table 6, taking into account the distribution of plutonium obtained by EPMA has only a relatively poor influence on the fit. Even if the difference curve of the pattern fitted with 11 phases (Figure 5a) evidence a better fit than that of the pattern refined with only one phase (Figure 5b), the improvement remains minor. Thus, considering the material as monophasic is justified because the cation distribution heterogeneity of the present samples has only a slight effect on the fit result of XRD patterns.

Determination of Short-Range Structural Properties. XANES spectra collected on $U_{0.750}Pu_{0.246}Am_{0.004}O_{2-x}$ samples for U, Pu, and Am cations are compared to reference compounds (Figure 6) and fitted with a linear combination of the latter to determine the oxidation state of the constituting cations, so the O/M ratio, of the samples sintered under the three investigated conditions (Table 7).

Both uranium-L_{III} and americium-L_{II} XANES showed no variation with the sintering atmosphere, and U and Am cations remained purely tetravalent and trivalent, respectively. Such a behavior first confirms the fact that no U(V) is obtained under reducing atmosphere and, regarding the americium content of the present samples, also confirms the proposed Am(III)−U(IV) coexistence.[22,23] A different behavior was observed for plutonium cations with a slight shift of both white line maxima and first inflection point of Pu-L_{III} XANES to a lower energy when decreasing the oxygen potential of the sintering atmosphere. Thus, a partial reduction of Pu(IV) to Pu(III) was clearly evidenced.

To summarize, deviation from stoichiometry is endorsed by first, a complete reduction of Am(IV) to Am(III), then a partial reduction of Pu(IV) to Pu(III), whereas uranium remains purely tetravalent within all the samples. These results are consistent with our previous findings on $Pu_{1-y}Am_yO_{2-x}$ compounds[24] and confirm the model proposed by Osaka et al.,[22,23] which suggests the coexistence of Am(III) and U(IV) for the considered range of americium content.

Because deviations from stoichiometry were evidenced for all samples, EXAFS spectra were analyzed in order to gain information on the location of the lattice defects and/or to

DOI: 10.1021/acs.inorgchem.5b02533
Inorg. Chem. 2016, 55, 2123−2132

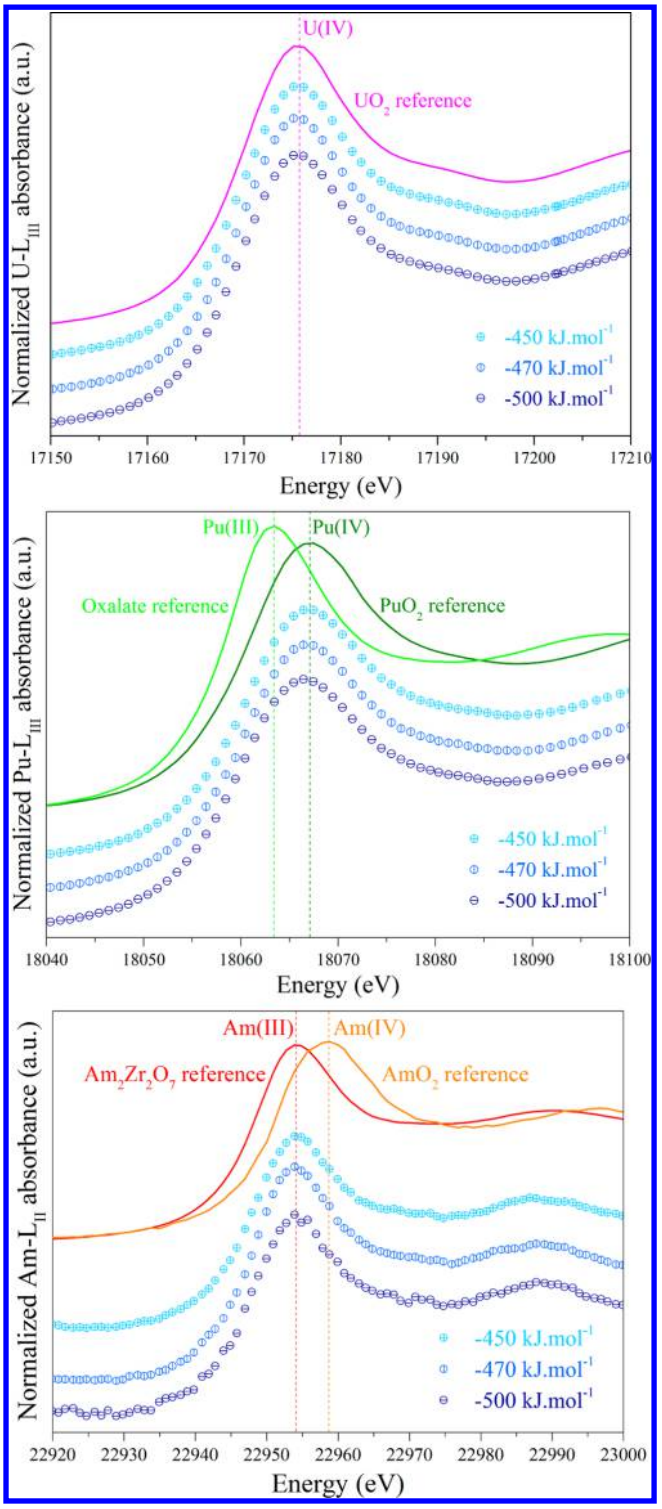

Figure 6. XANES spectra at U-L_{III}, Pu-L_{III}, and Am-L_{II} edges collected on $U_{0.750}Pu_{0.246}Am_{0.004}O_{2-x}$ samples sintered under the three atmospheres compared with reference compounds (solid lines).

highlight a possible clustering effect within the fluorite structure. Local environments around uranium and plutonium cations are compared in Figure 7, and associated fit results are given in Table 8.

The lack of modifications observed around U atoms as a function of O/M ratio matches the fixed U(IV) valence determined from XANES spectra. The Pu−O distances being in all cases smaller than that of U−O, the presence of Pu(IV),

Table 7. Plutonium cations percentage and O/M ratio calculated from the XANES analysis

oxygen potential at 2023 K (kJ mol^{-1})	Pu cation distribution (wt %)		calculated O/M ratio
	Pu(III)	Pu(IV)	
−450	8(2)	92(2)	1.99(1)
−470	12(2)	88(2)	1.98(1)
−500	20(2)	80(2)	1.97(1)

which has an ionic radius smaller than that of U(IV) in 8-fold-coordination,[53] in major quantity is confirmed. However, a slight increase in the Pu−O distances (first shell) is observed when decreasing the oxygen potential of the sintering gas mixture at 2023 K. As mentioned by Vigier et al.,[32] this increase in the Pu−O distances is due to the occurrence of Pu(III) in the fluorite structure because its estimated ionic radius in 8-fold-coordination is larger than that of both Pu(IV) and U(IV).[54,55] Moreover, this variation in the Pu−O distances is combined to an intensity decrease of the EXAFS oscillations, which is particularly visible with the associated Fourier transforms for distances greater than 5 Å. Such an evolution is not observed at the U-L_{III} edge. Thus, this increase in the lattice disorder can be notably related to different Pu(III)−O and Pu(IV)−O distances. No additional cation−cation distances based on lattice parameter distribution, as detailed in Table 5, were introduced. The differences between these distances are below the EXAFS uncertainties, and taking into account the hypothetical intermediate $U_{1-y}Pu_yO_2$ solid solutions from Table 5 would only have an effect on the evolution of the Debye−Waller factors as an increase of lattice disorder.

Comparison of the Characterization Techniques. Because of the different depths that gravimetry, XRD, and XANES are able to probe, the O/M ratios determined from each method will be different and their comparison informative (Figure 8). For clarity reasons, error bars associated with the determination of O/M ratios are only given in the legend.

Regardless of the characterization method, the increase in the oxygen potential at 2023 K leads to a higher O/M ratio of the $U_{0.750}Pu_{0.246}Am_{0.004}O_{2-x}$ mixed oxide at room temperature. However, even when taking into account error bars, evident discrepancies are noticeable between the three techniques as a consequence of the different probed depths. Furthermore, as shown in ref 21, this comparison provides important information about both kinetics and extent of the expected oxidation at room temperature. Indeed, for a given oxygen potential at 2023 K, the difference between the O/M ratios determined by gravimetry, XRD, and XANES is reduced when increasing the oxygen potential (i.e., when the O/M ratio of the sample is higher). This provides evidence for the role of the surface in the oxidation process and highlights the fact that a more hypostoichiometric sample oxidizes faster at room temperature. This is also in agreement with results provided by Woodley et al.[56]

Effect of Homogeneity of Cation Distribution. In a previous study of $U_{0.54}Pu_{0.45}Am_{0.01}O_{2-x}$ samples with high homogeneity of cation distribution, we have shown that trivalent plutonium fully reoxidizes to Pu(IV) in the time-lapse separating preparation and analysis of the samples.[21] We have also shown that, for a given sintering step (temperature, atmosphere, dwell duration, and heating/cooling rates), the homogeneity of cation distribution has a clear influence on the oxidation state of the constitutive actinides.[17] More precisely, the presence of local

DOI: 10.1021/acs.inorgchem.5b02533
Inorg. Chem. 2016, 55, 2123−2132

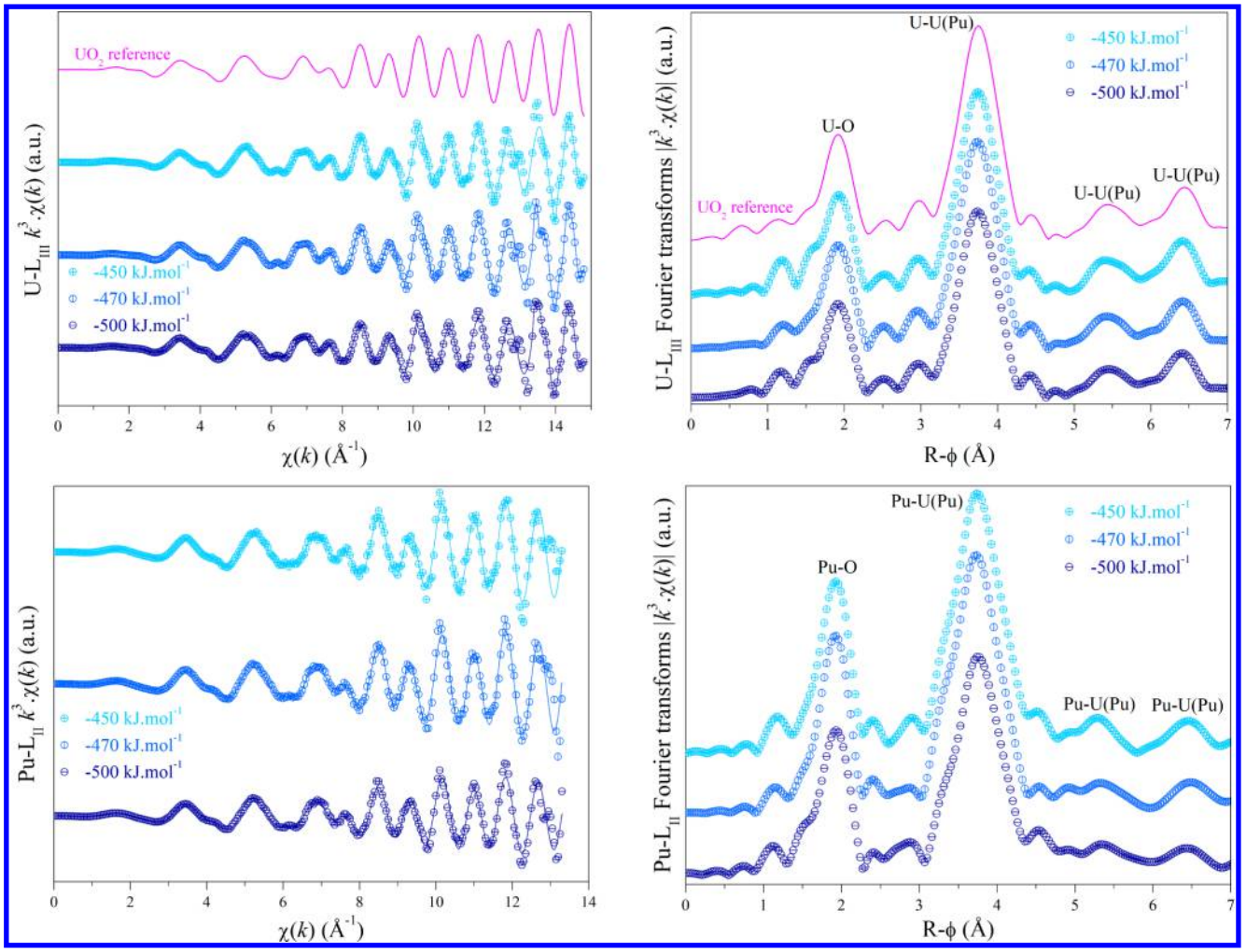

Figure 7. Experimental and fitted EXAFS spectra collected on $U_{0.750}Pu_{0.246}Am_{0.004}O_{2-x}$ samples sintered under the three atmospheres compared with reference compound (solid line) and respective Fourier transforms.

$(Pu,Am)O_{2-x}$ high concentrations lead to more hypostoichiometric compounds as compared to more homogeneous samples. In addition, mixed oxides with a high cation distribution homogeneity also seem to spontaneously reoxidize more readily at room-temperature.[17,21] Because the $U_{0.750}Pu_{0.246}Am_{0.004}O_{2-x}$ samples of this study have a lower homogeneity of cation distribution than the mixed oxides investigated in reference,[21] they have a lower initial O/M ratio. We believe this observation emphasizes the correlation between deviation from stoichiometry, homogeneity of cation distribution, actinide oxidation states, and kinetics of room-temperature oxidation. Similarly to the present study, a lower homogeneity of cation distribution than that of samples from reference[21] might explain why Vigier et al.[32] have managed to determine low O/M ratios from XAS experiments without observing a fast reoxidation at room temperature. Finally, the fabrication of Am-bearing uranium−plutonium mixed oxides studied by Osaka et al.[22,23] is thoroughly described in refs 57,58. These samples were elaborated by a conventional powder metallurgy route and also evidenced significant heterogeneity of cation distribution likely to affect their O/M ratio. This might also have implications on the observed discontinuities in the oxygen potential versus O/M ratio curves reported by the authors.

Outlooks. The upcoming step will be to study Am-bearing (~5%) uranium−plutonium mixed oxides in order to evaluate the effect of a higher americium content on both O/M ratio and its variation with the oxygen potential. That will allow verifying the reported observations of Am(IV)−U(IV) interactions leading to the Am(III)−U(V) coexistence as well as the accuracy of the thermodynamic description proposed by Osaka et al.[22,23]

4. CONCLUSION

The present study shows that in hypostoichiometric $U_{0.750}Pu_{0.246}Am_{0.004}O_{2-x}$ mixed oxide samples, the reduction of Am(IV) to Am(III) is completed before any reduction of Pu(IV) cations is observed. Moreover, uranium cations remain tetravalent regardless of the investigated sintering gas mixture. We believe that the discrepancies between various studies found in the literature most likely result from different homogeneities of cation distribution within the samples.

AUTHOR INFORMATION

Corresponding Author

*E-mail: philippe-m.martin@cea.fr. Tel.: +33 4 42 25 33 08.

Notes

The authors declare no competing financial interest.

ACKNOWLEDGMENTS

The authors are pleased to acknowledge Dr. J. Léchelle, Dr. M. Strach, Mr. Y. Marc, Mr. J.-C. Richaud, Mr. A. Arredondo, Mr. P.

DOI: 10.1021/acs.inorgchem.5b02533
Inorg. Chem. 2016, 55, 2123−2132

Table 8. Structural Parameters Extracted by Fitting EXAFS Spectra Measured at Both U-L_{III} and Pu-L_{II} Edges Compared to Those Determined by XRD

	EXAFS					XRD
sample	edge	coordination shell	N	R (Å)	σ^2 (Å^2)	R (Å)
UO_2 reference	U-L_{III}	O	8.0(5)	2.365(5)	0.0035(5)	2.369
		U	12.0(5)	3.86(1)	0.0013(5)	3.868
		O	24(2)	4.54(1)	0.006(2)	4.536
PuO_2 reference	Pu-L_{II}	O	8.0(5)	2.335(1)	0.0063(5)	2.336
		Pu	12.0(5)	3.81(1)	0.0028(5)	3.816
		O	24(2)	4.47(2)	0.007(2)	4.474
−450 kJ mol^{-1}	U-L_{III}	O	8.0(5)	2.358(5)	0.0041(5)	2.362
		M	12.0(5)	3.85(1)	0.0018(5)	3.858
		O	24(2)	4.53(2)	0.006(2)	4.524
	Pu-L_{II}	O	8.0(5)	2.346(5)	0.0038(5)	2.362
		M	12.0(5)	3.85(1)	0.0016(5)	3.858
		O	24(2)	4.48(2)	0.005(2)	4.524
−470 kJ mol^{-1}	U-L_{III}	O	8.0(5)	2.357(5)	0.0039(5)	2.363
		M	12.0(5)	3.85(1)	0.0017(5)	3.859
		O	24(2)	4.52(2)	0.005(2)	4.525
	Pu-L_{II}	O	8.0(5)	2.342(5)	0.0032(5)	2.363
		M	12.0(5)	3.85(1)	0.0015(5)	3.859
		O	24(2)	4.50(2)	0.007(5)	4.525
−500 kJ mol^{-1}	U-L_{III}	O	8.0(5)	2.356(5)	0.0045(5)	2.364
		M	12.0(5)	3.85(1)	0.0020(5)	3.861
		O	24(2)	4.53(2)	0.005(5)	4.524
	Pu-L_{II}	O	8.0(5)	2.352(5)	0.0055(5)	2.364
		M	12.0(5)	3.85(1)	0.0025(5)	3.861
		O	24(2)	4.49(2)	0.006(5)	4.527

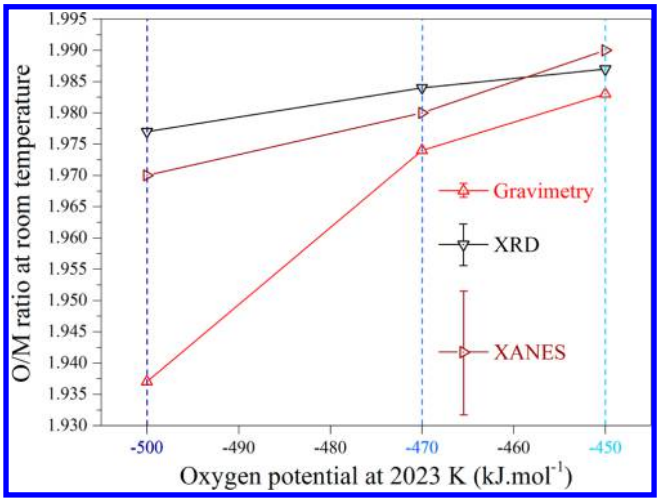

Figure 8. O/M ratios at room temperature determined by means of gravimetry, XRD, and XANES as a function of the oxygen potential at 2023 K.

Beaugelin, Mr. T. Dubois, Mrs. I. Felines, and Mrs. M.-A. Salaman-Martinez for their precious contributions to this work. The Global Actinide Cycle International Demonstration (GACID) project connecting the Commissariat à l'Energie Atomique et aux énergies alternatives (France), the Department Of Energy (U.S.A.), and the Japan Atomic Energy Agency (Japan) is also to be acknowledged for financial support. The authors would also like to acknowledge the European Synchrotron Radiation Facility (ESRF, Grenoble, France) for provision of synchrotron facilities at BM20 - Rossendorf Beamline.

REFERENCES

(1) Pillon, S. In *Comprehensive Nuclear Materials*; Konings, R. J. M., Ed.; Elsevier: Oxford, 2012; pp 109−141.
(2) Wakabayashi, T.; Takahashi, K.; Yanagisawa, T. *Nucl. Technol.* **1997**, *118*, 14−25.
(3) Salvatores, M.; Zaetta, A.; Girard, C.; Delpech, M.; Slessarev, I.; Tommasi, J. *Appl. Radiat. Isot.* **1995**, *46*, 681−687.
(4) Warin, D. *J. Nucl. Sci. Technol.* **2007**, *44*, 410−414.
(5) Ganev, I. K.; Lopatkin, A. V.; Orlov, V. V. *At. Energy* **2000**, *89* (5), 874−879.
(6) Konings, R. J. M.; Bakker, K.; Boshoven, J. G.; Hein, H.; Huntelaar, M. E.; van der Laan, R. R. *J. Nucl. Mater.* **1999**, *274*, 84−90.
(7) Chauvin, N.; Konings, R. J. M.; Matzke, H. *J. Nucl. Mater.* **1999**, *274*, 105−111.
(8) Croixmarie, Y.; Abonneau, E.; Fernández, A.; Konings, R. J. M.; Desmoulière, F.; Donnet, L. *J. Nucl. Mater.* **2003**, *320*, 11−17.
(9) Mayer, K.; Kanellakopoulos, B.; Naegele, J.; Koch, L. *J. Alloys Compd.* **1994**, *213-214*, 456−459.
(10) Delahaye, T.; Lebreton, F.; Horlait, D.; Herlet, N.; Dehaudt, P. *J. Nucl. Mater.* **2013**, *432*, 305−312.
(11) Beauvy, M. *J. Nucl. Mater.* **1992**, *188*, 232−238.
(12) Philipponneau, Y. *J. Nucl. Mater.* **1992**, *188*, 194−197.
(13) Duriez, C.; Alessandri, J.-P.; Gervais, T.; Philipponneau, Y. *J. Nucl. Mater.* **2000**, *277*, 143−158.
(14) Vaudez, S.; Belin, R. C.; Aufore, L.; Sornay, P.; Grandjean, S. *J. Nucl. Mater.* **2013**, *442*, 227−234.
(15) Berzati, S.; Vaudez, S.; Belin, R. C.; Léchelle, J.; Marc, Y.; Richaud, J.-C.; Heintz, J.-M. *J. Nucl. Mater.* **2014**, *447*, 115−124.
(16) Vaudez, S.; Léchelle, J.; Berzati, S.; Heintz, J.-M. *J. Nucl. Mater.* **2015**, *460*, 221−225.
(17) Vauchy, R.; Robisson, A.-C.; Martin, P. M.; Belin, R. C.; Aufore, L.; Scheinost, A. C.; Hodaj, F. *J. Nucl. Mater.* **2015**, *456*, 115−119.
(18) Vauchy, R.; Belin, R. C.; Robisson, A.-C.; Hodaj, F. *MRS Online Proc. Libr.***2014**, Vol. *1645*, DOI: 10.1557/opl.2014.89.
(19) Vauchy, R.; Belin, R. C.; Robisson, A.-C.; Hodaj, F. *J. Eur. Ceram. Soc.* **2014**, *34*, 2543−2551.

DOI: 10.1021/acs.inorgchem.5b02533
Inorg. Chem. 2016, 55, 2123−2132

(20) Vauchy, R.; Belin, R. C.; Robisson, A.-C.; Hodaj, F. *J. Nucl. Mater.* **2016**, *469*, 125−132.
(21) Vauchy, R.; Robisson, A.-C.; Belin, R. C.; Martin, P. M.; Scheinost, A. C.; Hodaj, F. *J. Nucl. Mater.* **2015**, *465*, 349−357.
(22) Osaka, M.; Namekawa, T.; Kurosaki, K.; Yamanaka, S. *J. Nucl. Mater.* **2005**, *344*, 230−234.
(23) Osaka, M.; Kurosaki, K.; Yamanaka, S. *J. Alloys Compd.* **2007**, *428*, 355−361.
(24) Belin, R. C.; Martin, P. M.; Léchelle, J.; Reynaud, M.; Scheinost, A. C. *Inorg. Chem.* **2013**, *52*, 2966−2972.
(25) Woodley, R. E. *Equilibrium oxygen potential-composition relations in hypostoichiometric plutonia*; HEDL-SA-1830; Hanford Engineering Development Laboratory: Richland, WA, 1979.
(26) Nishi, T.; Nakada, M.; Suzuki, C.; Shibata, H.; Okamoto, Y.; Akabori, M.; Hirata, M. *J. Nucl. Mater.* **2011**, *418*, 311−312.
(27) Prieur, D.; Martin, P. M.; Jankowiak, A.; Gavilan, E.; Scheinost, A. C.; Herlet, N.; Dehaudt, P.; Blanchart, P. *Inorg. Chem.* **2011**, *50*, 12437−12445.
(28) Prieur, D.; Martin, P.; Lebreton, F.; Delahaye, T.; Banerjee, D.; Scheinost, A. C.; Jankowiak, A. *J. Nucl. Mater.* **2013**, *434* (1−3), 7−16.
(29) Lebreton, F.; Belin, R. C.; Delahaye, T.; Blanchart, P. *J. Solid State Chem.* **2012**, *196*, 217−224.
(30) Belin, R. C.; Martin, P. M.; Valenza, P. J.; Scheinost, A. C. *Inorg. Chem.* **2009**, *48*, 5376−5381.
(31) Lebreton, F.; Martin, P. M.; Horlait, D.; Bès, R.; Scheinost, A. C.; Rossberg, A.; Delahaye, T.; Blanchart, P. *Inorg. Chem.* **2014**, *53* (18), 9531−9540.
(32) Vigier, J.-F.; Martin, P. M.; Martel, L.; Prieur, D.; Scheinost, A. C.; Somers, J. *Inorg. Chem.* **2015**, *54*, 5358−5365.
(33) Vauchy, R.; Robisson, A.-C.; Audubert, F.; Hodaj, F. *Ceram. Int.* **2014**, *40* (7, Part B), 10991−10999.
(34) Chase, Jr., M. W. *NIST-JANAF Thermochemical Tables*, 4th ed.; National Institute of Standards and Technology: Gaithersburg, Maryland, 1998; Vol. Monograph No. *9*.
(35) Oudinet, G.; Munoz-Viallard, I.; Aufore, L.; Gotta, M.-J.; Becker, J. M.; Chiarelli, G.; Castelli, R. *J. Nucl. Mater.* **2008**, *375*, 86−94.
(36) Guéneau, C.; Dupin, N.; Sundman, B.; Martial, C.; Dumas, J.-C.; Gossé, S.; Chatain, S.; Bruycker, F. D.; Manara, D.; Konings, R. J. M. *J. Nucl. Mater.* **2011**, *419*, 145−167.
(37) Moore, E.; Guéneau, C.; Crocombette, J.-P. *J. Solid State Chem.* **2013**, *203*, 145−153.
(38) Belin, R. C.; Valenza, P. J.; Reynaud, M. A.; Raison, P. E. *J. Appl. Crystallogr.* **2004**, *37*, 1034−1037.
(39) Pawley, G. S. *J. Appl. Crystallogr.* **1981**, *14*, 357−361.
(40) Bruker AXS GmbH. *TOPAS V4: General Profile and Structure Analysis Software for Powder Diffraction Data, User's Manual*; Bruker AXS GmbH: Karlsruhe, Germany, 2008.
(41) Martin, P.; Grandjean, S.; Valot, C.; Carlot, G.; Ripert, M.; Blanc, P.; Hennig, C. *J. Alloys Compd.* **2007**, *444*−*445*, 410−414.
(42) Ravel, B.; Newville, M. *J. Synchrotron Radiat.* **2005**, *12*, 537−541.
(43) Kvashnina, K. O.; Kvashnin, Y. O.; Butorin, S. M. *J. Electron Spectrosc. Relat. Phenom.* **2014**, *194*, 27−36.
(44) Böhler, R.; Welland, M. J.; Prieur, D.; Cakir, P.; Vitova, T.; Pruessmann, T.; Pidchenko, I.; Hennig, C.; Guéneau, C.; Konings, R. J. M.; Manara, D. *J. Nucl. Mater.* **2014**, *448*, 330−339.
(45) Conradson, S. D.; Begg, B. D.; Clark, D. L.; den Auwer, C.; Ding, M.; Dorhout, P. K.; Espinosa-Faller, F. J.; Gordon, P. L.; Haire, R. G.; Hess, N. J.; Hess, R. F.; Webster Keogh, D.; Lander, G. H.; Manara, D.; Morales, L. A.; Neu, M. P.; Paviet-Hartmann, P.; Rebizant, J.; Rondinella, V. V.; Runde, W.; Drew Tait, C.; Kirk Veirs, D.; Villella, P. M.; Wastin, F. *J. Solid State Chem.* **2005**, *178*, 521−535.
(46) Martin, P.; Grandjean, S.; Ripert, M.; Freyss, M.; Blanc, P.; Petit, T. *J. Nucl. Mater.* **2003**, *320* (1−2), 138−141.
(47) Arab-Chapelet, B.; Martin, P. M.; Costenoble, S.; Delahaye, T.; Scheinost, A. C.; Grandjean, S.; Abraham, F. *Dalton Trans.*
(48) Rehr, J. J.; Albers, R. C. *Rev. Mod. Phys.* **2000**, *72*, 621−654.
(49) Sundman, B.; Jansson, B.; Andersson, J.-O. *CALPHAD: Comput. Coupling Phase Diagrams Thermochem.* **1985**, *9*, 153−190.
(50) Vauchy, R.; Robisson, A.-C.; Bienvenu, P.; Roure, I.; Hodaj, F.; Garcia, P. *J. Nucl. Mater.* **2015**, *467* (Part 2), 886−893.
(51) Strach, M.; Belin, R. C.; Richaud, J.-C.; Rogez, J. *J. Phys. Chem. C* **2015**, *119*, 23159−23167.
(52) Belin, R. C.; Strach, M.; Truphémus, T.; Guéneau, C.; Richaud, J.-C.; Rogez, J. *J. Nucl. Mater.* **2015**, *465*, 407−417.
(53) Shannon, R. D. *Acta Crystallogr., Sect. A: Cryst. Phys., Diffr., Theor. Gen. Crystallogr.* **1976**, *32*, 751−767.
(54) Kato, M.; Konashi, K. *J. Nucl. Mater.* **2009**, *385*, 117−121.
(55) Kinoshita, H. In *Handbook of Advanced Radioactive Waste Conditioning Technologies*; Ojovan, M. I., Ed.; Woodhead Publishing Series in Energy; Woodhead Publishing: Cambridge, U.K., 2011; pp 293−338.
(56) Woodley, R. E.; Gibby, R. L. *Room-temperature oxidation of (U,Pu) O2-x*; HEDL-SA-592, CONF-731041-6; Hanford Engineering Development Laboratory: Richland, WA, 1973.
(57) Miwa, S.; Osaka, M.; Yoshimochi, H.; Tanaka, K.; Seki, T.; Sekine, S. *Effect of oxygen potential on the sintering behavior of MOX fuel containing Am.*; JNC TN9400 2005-023; Japan Nuclear Cycle Development Institute: Ibaraki, Japan2005.
(58) Yoshimochi, H.; Nemoto, M.; Mondo, K.; Koyama, S.; Namekawa, T. *J. Nucl. Sci. Technol.* **2004**, *41*, 850−856.

DOI: 10.1021/acs.inorgchem.5b02533
Inorg. Chem. 2016, 55, 2123−2132